Gold-black manufacture, microstructure, and optical characterization

Nazia B. Munir,[1] **J. R. Mahan,**[1,*] **Luan C. Doan,**[1] **N. Q. Vinh,**[2] ⓘ **and Kory J. Priestley**[3]

[1]*Department of Mechanical Engineering, Virginia Tech, Blacksburg, Virginia 24061, USA*
[2]*Department of Physics and Center for Soft Matter and Biological Physics, Virginia Tech, Blacksburg, Virginia 24061, USA*
[3]*Climate Sciences Branch, NASA Langley Research Center, Hampton, Virginia 23682, USA*
Corresponding author: jrmahan@vt.edu

A previous contribution formulates a first-principle dipole antenna theory for predicting the polarization-sensitive directional spectral absorptance of gold-black in the near infrared. The current contribution chronicles a successful effort to validate that theory. After a brief review of gold-black history, we describe in some detail the design and construction of a vapor-deposition cell for laying down gold-black coatings on a mirrorlike gold substrate. The microstructure of 4- and 8-μm-thick coatings is revealed using scanning electron microscopy. An automated bench-level reflectometer has been used to measure the in-plane bidirectional reflectivity of the gold-black coatings in the visible (532 nm) and near-infrared (800 nm) for p and s polarization. Measurements are reported over incident zenith angles ranging between 10 and 50 deg. Results obtained using the apparatus are consistent with the dipole antenna theory in this range of incident zenith angles. © 2021 Optical Society of America

1. INTRODUCTION

In recent years, gold-black has emerged as the detector coating of choice for Earth radiation budget (ERB) monitoring applications. Already used in the European EarthCARE instrument [1], gold-black was considered for use in NASA's follow-up to CERES [2], the Radiation Budget Instrument (RBI) [3], before the latter was deselected. It is now under consideration for use in DEMETER [4], a next-generation NASA ERB initiative. The suitability of gold-black-coated thermistors and thermopiles for this application is based on the fact that they can be relatively insensitive to wavelength between the ultraviolet and the mid-range infrared and that, after suitable calibration, their performance can be predicted using well-understood first-principle models. Knowledge of the optical behavior of the absorbing coating is key to correctly interpreting heat flux measurements obtained by such detectors [1,2,5–8].

In a previous contribution we describe a first-principle dipole antenna theory for the polarization-sensitive directional spectral absorptance of gold-black in the near-infrared [9]. The current contribution represents an attempt to validate that theory through creation and optical characterization of gold-black coatings. One of the obstacles to gold-black research is limited access to gold-black samples. Because of its ephemeral and delicate nature, gold-black must be created on a surface from which it is then effectively inseparable. The absence of a commercially available apparatus for vapor depositing gold-black led to the design and fabrication of the in-house version described here. Because the microstructure of gold-black, and therefore

its optical properties, is known to vary significantly depending on manufacturing conditions, step-by-step directions for using the apparatus, hard won through a tedious trial-and-error process, are also reported here. Finally, we describe an in-house bench-level bidirectional reflectometer used to measure the in-plane bidirectional reflectance distribution function (BRDF) of the gold-black coatings. BRDF measurements validating the earlier theory [9] are reported for 4- and 8-μm-thick gold-black coatings in the visible (532 nm) and near-infrared (800 nm) for p and s polarization and over incident zenith angles ranging between 10 and 50 deg.

2. BRIEF REVIEW OF GOLD-BLACK HISTORY

The earliest mention of metal-black in the literature was apparently in 1930, when Pfund [5] reported the accidental discovery of a totally unexpected characteristic of bismuth. Normally, a smooth bright surface results when bismuth is evaporated from a hot tungsten filament in high vacuum and allowed to condense on a cold substrate. However, Pfund found that if the chamber pressure is raised to 0.25 torr in an inert atmosphere, the deposit takes the form of an intensely black and fluffy layer, which he named "bismuth-black." He observed that bismuth-black is quite opaque in the visible and infrared and, in fact, that it behaves very nearly like an ideal blackbody. Furthermore, he predicted that other metals should yield metal-blacks. In 1933 Pfund [6] extended his research to gold, copper, zinc, silver, lead, cadmium, nickel, antimony, tellurium, and selenium,

and demonstrated that they also produce metal-blacks. In the intervening years, metal-blacks have generated a great deal of interest in the scientific community, with gold-black gaining more attention due to its chemical stability.

Between 1948 and 1956, Harris *et al*. [10–14] reported a series of intensive investigations of the production and properties of gold-black. They explored the effect of pressure and purity of the inert atmosphere, the gold evaporation rate, and the distance between the melt and deposition surface and correlated these parameters with the resulting optical behavior [10]. They also studied the effect of trace oxygen in the otherwise inert atmosphere and observed the nanostructure in gold-black formation under different experimental conditions [10,11]. They point out that coatings created in a pure nitrogen environment have high absorptance in the infrared, while the presence of trace oxygen results in lower absorptance beyond a wavelength of about 1 µm while retaining high absorptance in the visible [10]. The vast dataset created by Harris *et al*. has been used by later investigators to establish and validate absorptance models [15].

In 1977–1978, O'Neill *et al*. [16,17] attempted to establish the relationship between the optical behavior of gold-black and the particulate nature of the material. They produced gold-black samples under several laboratory conditions and concluded that manufacturing conditions play a vital role for determining the particulate structure of the deposit and thus its optical properties. In general, the absorptance was observed to increase with decreasing particle size. Contributions subsequent to that of O'Neill *et al*. deal mainly with defining the process for the production of gold-black [18–23]. The cited authors observe that the microstructure and optical properties of gold-black depend highly on manufacturing parameters such as chamber pressure, substrate temperature, evaporation rate, and so forth. In 1992, Lang *et al*. [18] reported a comparative study of the absorptance of different metal-blacks resulting from different deposition processes.

Following the path of earlier investigators, Becker *et al*. [19,20] concentrated on gold-black manufacturing conditions and performed a thorough study of the suitability of gold-black for thermal detector coatings in the far infrared. While investigating the effects of chamber pressure on gold-black formation, they provide a useful detailed description of their experimental apparatus. They conclude that the absorptance of gold-black, while influenced by the deposition rate and thus the microstructure, depends strongly on the vacuum pressure. In our previous work [9] we argue that the inert body gas plays the essential role of moderating the speed of gold molecules, thus favoring sublimation over condensation on the substrate.

Lehman *et al*. [21] studied gold-black deposition on a freestanding pyroelectric detector substrate. They developed an empirical correlation between the nitrogen pressure inside the vacuum chamber during evaporation and the distance between the melt and the substrate. They propose a rule of thumb for determining the combination of chamber pressure and melt-to-substrate distance. From their observations they conclude that the higher the pressure inside the vacuum chamber, the lower the deposition rate. They also studied the spatial uniformity of the gold-black coating and observed its dependence on the deposition process.

Nelms and Dowson [22] contributed to the design of a gold-black production process that ensures repeatability of optical performance of the coating in the mid-infrared. They attempted to optimize the parameters affecting gold-black production such as gold-melt mass, chamber pressure during evaporation, evaporation rate, and substrate temperature. Through their experimental efforts, they were able to define an optimized gold-black production process leading to improved absorptance in the mid-infrared.

Like Nelms and Dowson, Ilias *et al*. [23] pursued the optimization of an apparatus for producing a gold-black coating with high absorptance over wavelengths ranging from the ultraviolet to the far infrared. While attempting to establish a correlation between the coating thickness and the absorptance of the deposit, they concluded that a critical thickness produces maximum absorptance.

Gold-black eventually emerged as a popular coating for space applications [24–28]. Wang *et al*. [24] report a deposition process for gold-black suitable for microbolometer applications. They compared the performance of the microbolometer with and without a gold-black absorption layer. Results revealed that a microbolometer coated with a gold-black absorption layer exhibits improved performance without incurring a significant increase in thermal mass and thus a slower response time. They also studied the effect of the chamber pressure on gold-black formation and concluded that it influences the density and porosity of the gold-black layer.

Panjwani *et al*. [26–28] also investigated the applicability of gold-black for enhancing the absorptance of uncooled infrared detectors such as microbolometers. They used a stencil mask to create patterned gold-black layers to address the difficulty of integrating the extremely fragile gold-black coating with the microbolometer array. SEM images demonstrate that the patterned gold-black layer is denser than that obtained in the unmasked gold-black deposition process [27]. However, while this process preserves the absorptance of gold-black in the long wavelength infrared (LWIR), it does not improve performance in the middle wavelength infrared (MWIR). They suggest a new design using patterned gold-black, obtained by using a lift-off technique. A vapor-deposited SiO_2 protective layer does not significantly diminish the high absorptance in either the MWIR or the LWIR [28].

Ng *et al*. [29] investigated the applicability of gold-black in photonic-related applications such as solar fuel production, photodetectors, and photovoltaic devices. They developed a model to explain the surface property of gold-black in which they consider gold-black deposits consisting of nanotubes having high aspect ratios. According to their model, these tapered nanotubes are responsible for a graded refractive index that suppresses Fresnel reflection over a broad wavelength range. They also suggest that Fabry–Perot resonances of gap-plasmon modes between the nanotubes are responsible for the suppression of reflections. They develop a finite-element model for their nanostructure in an effort to validate their theory.

3. MANUFACTURE OF GOLD-BLACK COATINGS

The manufacture of metal-blacks has changed little since the early 1930s when Pfund first produced bismuth-black by

Table 1.   Gold-Black Manufacturing Conditions Reported in the Literature

Source	Substrate Temperature (°C)	Chamber Pressure (torr)	Inert Body Gas	Evaporation Rate (mg/s)	Melt-to-Substrate Distance (cm)	Wavelength (μm)	Substrate Material
Becker et al. [19,20]	−10	0.750–11.25	Nitrogen	0.7, 1	5		Cellulose nitrate films
Ilias et al. [23]		0.75–7.5	Nitrogen		9		
Nelms et al. [22]	−55	7.5	Nitrogen		10	Visible to mid Infra-red < 40	Chromium and gold coated glass
Harris et al. [10–14]		0.97508	Nitrogen	Between 0.5 & 3.3	7	100	Cellulose nitride film
O'Neill et al. [16,17]		1–20	Helium			0.35–2.4	
Lang et al. [18]		0.75	Argon/Nitrogen		6	2–20	Glass, silicon, silicon oxide, silicon nitride, aluminum, ceramics and epoxy
Panjwani et al. [26–28]	−13	1st: below 10^{-5} 2nd: back-filled to 0.30–3.00	Nitrogen		10	2–125	Polished silicon substrate
Lehman et al. [21]		1st: 3.75×10^{-6} 2nd: Coat at 0.975 & 1.95			3	1–20	Nickel-coated $LiTaO_3$, $LiNbO_3$ plate
Qian et al. [25]		1.50012		3.3	5	9	

evaporating pure bismuth from an electrically heated tungsten coil *in vacuo* and allowing it to sublimate on a cold surface [5]. In general, the process involves evaporation of a noble metal in a vacuum ranging from 0.01 to 0.1 torr and then allowing its vapor to sublimate on a cold surface. A suitable vacuum chamber having a low leakage rate is required. Under high vacuum, evaporated metal molecules travel with high kinetic energy in a straight line until they encounter a surface where they condense into a smooth shiny surface. However, as explained in Ref. [9], if the vacuum chamber is back-filled with inert gas, the speed of the metal molecules is moderated by collisions with the inert gas molecules. When the chamber back pressure and the melt-substrate distance are sufficient, the molecular flow transitions from momentum-dominated to diffusion-dominated, thus favoring sublimation and the formation of crystal-like dendrites on the surface. On a macroscopic level, the resulting coating appears to be a fuzzy black layer, resembling black hoarfrost.

Several gold-black investigators [5–8,10–29] have observed that the overall conditions during the evaporation process; such as gold quantity, chamber pressure, evaporation rate, substrate temperature, melt-substrate distance, and type of inert gas, influence the microstructure of the deposited coating. Different microstructures result in different coating optical behavior as evidenced by its absorptance, reflectivity, and transmissivity. Generally, gold-black shows good absorptance in the visible and near-infrared; however, depending on the manufacturing conditions, wide variations in absorptance are observed. Therefore, determining the appropriate manufacturing conditions that maximize absorptance over a desired wavelength range is of prime importance.

A. Design of the Gold-Black Manufacturing Process

A thorough and wide-ranging study of the pertinent literature was essential before undertaking the design of a gold-black manufacturing cell. While information concerning the choice of an inert body gas, chamber pressure, melt-to-substrate distance (and geometry), substrate temperature, and evaporation rate is widely available, it is spread across many sources, is occasionally contradictory, and is generally reticent on the actual step-by-step manufacturing procedure. Choosing the point of departure for the design and the critical operating parameters proved to be a challenging task. The extant literature provides a dauntingly wide range of manufacturing conditions, each producing an equally wide variety of coating microstructures and optical behavior. However, careful study of the literature permits identification of the key parameters and procedures that play a significant role in determining the microstructure and optical behavior:

1. Choice of inert body gas
2. Procedure for purging the chamber of oxygen
3. Evaporation pressure
4. Evaporation rate profile
5. Substrate material
6. Substrate temperature
7. Melt-to-substrate distance
8. Orientation of the substrate *vis-à-vis* the melt

Conditions gleaned from the literature, summarized in Table 1, provide guidelines for the design and operation of an apparatus for the manufacture of gold-black. The many empty

cells in Table 1 are testimony to the sparsity of detail about gold-black manufacturing available in the open literature.

B. Description of the Gold-Black Manufacturing Cell

In the absence of a suitable off-the-shelf gold-black manufacturing cell, we purchased and modified a commercially available apparatus (MTI Model GDL-1700X-SPC-2) intended for vacuum depositing noble metals such as gold and silver onto suitable substrates to create mirrorlike coatings. The original apparatus consisted of a thick-walled 6-in-ID quartz vacuum chamber evacuated by a two-stage rotary-vane vacuum pump. Unable to achieve the required vacuum using the original pump, we eventually replaced it with a compact two-stage turbo-molecular vacuum pump (Pfeiffer HICUBE 300 ECO). The vacuum chamber is mounted on a chassis that houses, among other functions, a nitrogen flow control valve and a programmable filament current controller. The shutter and substrate rotation drive required for the vapor-deposition process were removed, and the original vacuum-chamber lid was replaced.

In the original design, pure gold pellets were melted and evaporated in a small alumina crucible wrapped with a tungsten filament and mounted within a miniature ceramic oven. The evaporation rate produced by this arrangement proved to be inadequate for gold-black production. Therefore, following the indications given in Refs. [10–14,16–18,22], we replaced the oven and crucible with a free-standing V-shaped tungsten filament wrapped with a 0.5-mm-diameter pure gold wire whose length determined the thickness of the eventual gold-black coating. We also abandoned the programmed filament current controller in favor of manual control. A photograph of the modified manufacturing cell appears in Fig. 1(a).

Several references cite the need for careful control of the substrate temperature [19,20,22,26–28]. Therefore, because the original apparatus lacked a means for controlling the substrate temperature, we modified the vacuum chamber lid to permit the passage of coolant tubes to and from the specially designed cold finger shown in Fig. 1(b). The temperature of the coolant (automotive antifreeze) is controlled by an external circulating chiller (Across International C15-3-2 L) capable of supplying coolant at temperatures as low as $-15°C$ at a flow rate of up to 17 L/min.

Various substrate materials were investigated including cellophane tape, glass microscope slides and slide covers, aluminum foil, gold foil, copper, and gold-plated silicon wafers. In the end, while gold-black forms on and adheres to all of these materials, we used gold-plated silicon wafers in the current effort because
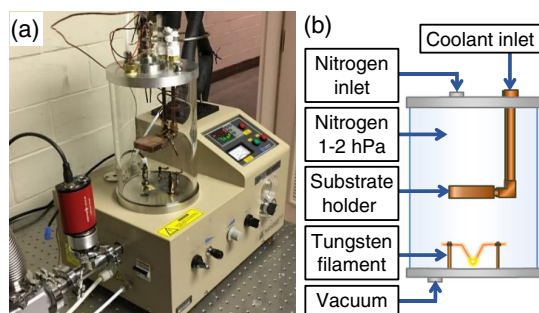

Fig. 1.   Gold-black manufacturing cell.

of their smooth mirror-like surface finishes. Finally, following the preponderance of other investigators, the chamber is backfilled to the desired pressure with ultrapure nitrogen after a 12-hr high-vacuum purge of the chamber.

C. Gold-Black Manufacturing Procedure

In this section we describe the gold-black manufacturing process in sufficient detail to allow reproduction of the results presented here. The process may be divided into two parts: substrate preparation and sample preparation.

1. Substrate Preparation

Gold-black can be deposited on virtually any surface offering an adequate heat conduction path to the cold finger. Our samples were created by evaporative deposition of gold-black on 625-μm-thick, single-side-polished, n-doped, silicon wafers (University Wafer, ID #1025). Pure silicon is an excellent conductor of heat but is partially transparent in the near-IR. Because the BRDF measurement process requires that the gold-black coating be deposited on a mirrorlike surface at all wavelengths, a plasma vapor depositor (Kurt J Lesker PVD Model 250) was used to lay down a uniform thin layer of gold on the silicon wafer. Before applying a 100-nm-thick pure gold finish layer, the wafer was first coated with a 50-nm-thick chromium layer to enhance the adherence of the gold layer. The gold-plated silicon wafer was then carefully excised into small segments using a diamond stylus. The individual segments were then cleaned using a nitrogen jet to remove dust and any chip particles that may have been created during the excising process. Once thoroughly cleaned, the substrate segments were carefully stored in a sealed container.

2. Sample Preparation

Gold-black samples are produced in the vacuum chamber depicted in Fig. 1. The chamber must be carefully cleaned using denatured alcohol before each coating operation. Substrate segments are then taped along the edges to the downward-facing surface of the cold finger, and a 5-cm length of 0.5-mm diameter gold wire is wound around one of the "V"s of the tungsten filament. The vacuum chamber is then sealed and evacuated to a pressure of 2.25×10^{-5} torr. This hard vacuum is maintained for 12 hr to ensure the complete outgassing of oxygen, water vapor, and any other gaseous constituents. During the evacuation process circulation of coolant (automotive antifreeze) through the cold finger is delayed for a few hours to avoid the condensation in the chamber. The cold finger as well as the attached substrate segments eventually attain a temperature of $-12°C$.

After 12 hr of continuous pumping, ultrapure nitrogen is slowly bled into the vacuum chamber until a pressure of 1.65×10^{-2} torr is reached. The gate valve between the vacuum pump and the vacuum chamber is then closed, and the nitrogen flow into the chamber is carefully metered until a final pressure of 0.645 torr is attained.

Once the desired pressure has been achieved, the current flow through the tungsten filament is gradually increased at
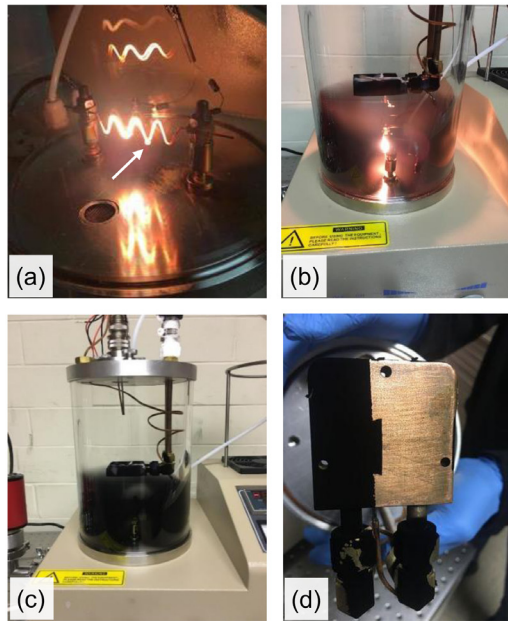
Fig. 2. (a) Gold wire wrapped on the electrically heated tungsten filament has melted for form a bead (arrow), (b) the onset of evaporation and gold-black formation, (c) the apparatus at the end of a gold-black manufacturing run, and (d) gold-black deposit formed on the bottom surface of the cold finger and a crescent-shaped sample (a second sample originally taped on the right-hand side has been removed).

an average rate of 0.118 A/min until the gold melts and forms a bead at the bottom of the "V" as illustrated in Fig. 2(a). The maximum heating rate is set by the controller provided with the commercial coater to protect the tungsten filament from fusing. The maximum current capacity of the tungsten filament is about 30 A. At this heating rate a little over 2 hr is required to attain the melting point of gold, which occurs at a filament current of about 24 A. Once the molten bead has formed, the filament current is increased to 26 A. At this point, gold evaporation and the formation of gold-black begins as illustrated in Fig. 2(b). Approximately 5 min is required to completely consume the gold bead. Figure 2(c) shows the apparatus at the end of a production run, and Fig. 2(d) shows the bottom surface of the cold finger with one on the samples still in place on the left-hand side. Once the production run has been completed, the tungsten filament is allowed to cool gradually by slowly reducing the current. The chiller circulating pump is turned off to allow the cold finger and gold-black to warm to room temperature. Once room temperature is attained, a vacuum bleed valve is slowly opened, allowing atmospheric air to enter the chamber, after which the chamber is opened and the gold-black samples carefully removed and stored. Table 2 is an extension of Table 1, summarizing the manufacturing conditions used in the current

effort. The fabrication method of gold-black materials is simple and cost-effective when compared with other techniques using laser deposition and/or electron beam lithography.

4. CHARACTERIZATION OF GOLD-BLACK SAMPLE MICROSTRUCTURE

Figure 3 shows plan and elevation views of SEM images of the 4- and 8-μm-thick gold-black deposits. The plan views are reminiscent of aerial views of deciduous forests observed from different altitudes. Noteworthy is the evolution in texture size scale with sample thickness evident from comparison of Figs. 3(a) and 3(d). The initial stage of growth favors the emergence of tightly packed gold-black "shrubs," as seen in Fig. 3(a), corresponding to a layer thickness of about 4 μm. As growth continues, these initial shrubs compete for nourishment by the "rain" of gold atoms, with those having a size advantage over their neighbors growing more rapidly and eventually choking out further growth by their smaller neighbors, just as occurs in a real forest. By the time the gold-black layer has reached a thickness of about 8 μm (under the current growing conditions), the individual "trees" have merged to form a relatively homogeneous canopy. These images support the interpretation in Ref. [9] of gold-black morphology as a mossy array of fine gold filaments, which act as dipole antennas in the absorption process.

5. MEASUREMENT OF GOLD-BLACK BRDF

A. Definition of the Bidirectional Reflectance Distribution Function

The experimental results are presented in terms of the BRDF:

$$\text{BRDF} \equiv \frac{dI_{\lambda,r}(\lambda, \vartheta_i, \varphi_i, \vartheta_r, \varphi_r)}{I_{\lambda,i}(\lambda, \vartheta_i, \varphi_i)\cos\vartheta_i d\Omega_i}, \tag{1}$$

also commonly referred to as the bidirectional spectral reflectivity, $\rho_\lambda(\lambda, \vartheta_i, \varphi_i, \vartheta_r, \varphi_r)$ [30]. In Eq. (1), $I_{\lambda,i}(\lambda, \vartheta_i, \varphi_i)$ is the intensity in wavelength interval $d\lambda$ about wavelength λ incident to the sample from direction (ϑ_i, φ_i), where ϑ_i is the incident zenith angle measured with respect to the normal to the sample and φ_i is the azimuth angle; $d\Omega_i = dA_i/r^2$ is the solid angle surrounding direction (ϑ_i, φ_i), where dA_i is the area of the illuminated spot on the coupon; r is the distance from the light source to the illuminated spot; and $dI_{\lambda,r}(\lambda, \vartheta_i, \varphi_i, \vartheta_r, \varphi_r)$ is the intensity of the reflected beam in direction (ϑ_r, φ_r). The geometry and nomenclature corresponding to Eq. (1) appear in Fig. 4.

The BRDF has the dimensions of inverse solid angle and the units of inverse steradians (sr^{-1}). The experimental apparatus and procedure for measuring the quantity defined by Eq. (1) are

Table 2. Gold-Black Manufacturing Conditions in the Current Contribution

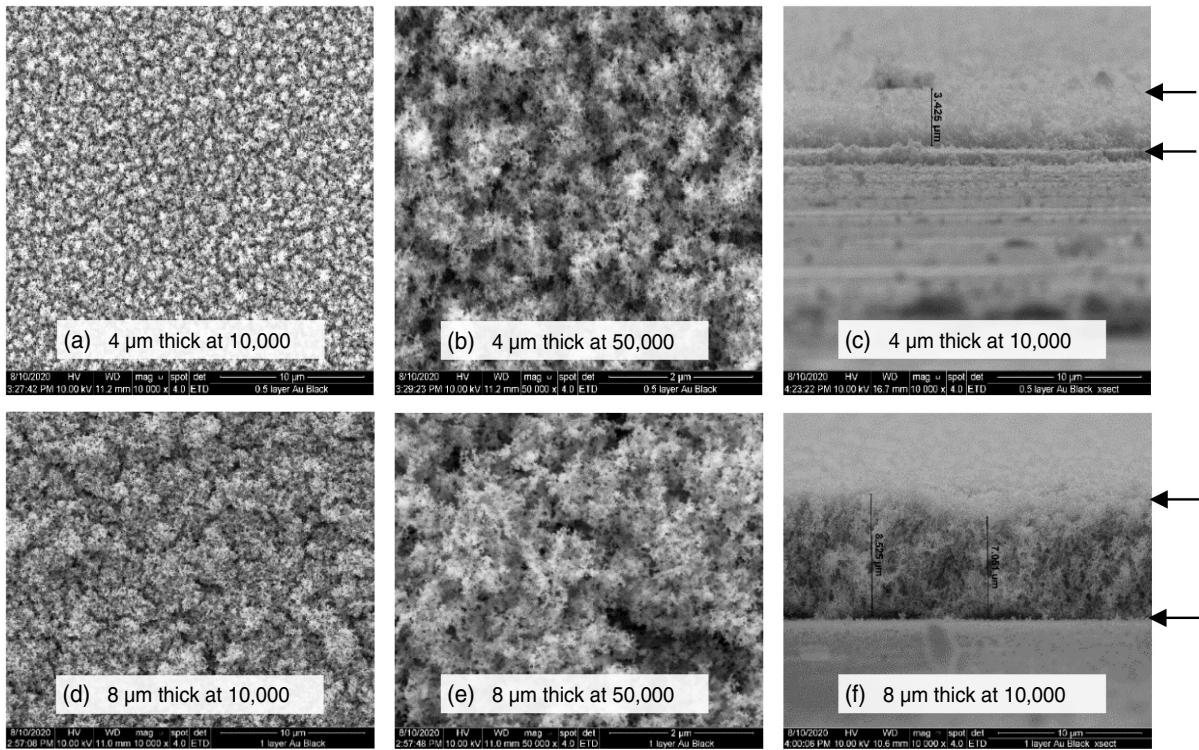| Gold Source	Substrate Temperature (°C)	Initial Vacuum Pressure (torr)	Chamber Pressure (torr)	Body Gas	Evaporation Rate (mg/s)	Melt-to-Substrate Distance (cm)	Substrate Material	Current Rate (A/min)
0.5 mm dia., 5-cm gold wire	−12	2.25×10^{-5}	0.645	N_2	0.010526	5	Gold-coated silicon wafer	0.118

Fig. 3. (a), (b), (d), (e) Plan and (c), (f) elevation SEM images (a), (b), (c) of an approximately 4-μm-thick sample of gold-black and (d), (e), (f) of an approximately 4-μm-thick sample of gold-black. The arrows indicate the top and bottom edges of the gold-black layers.
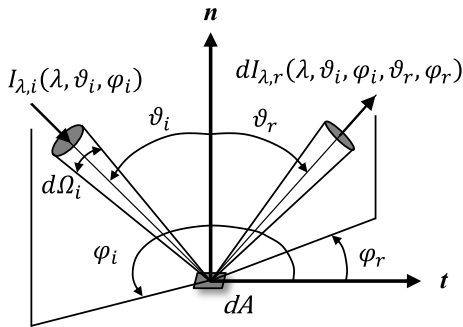

Fig. 4. Geometry and nomenclature corresponding to Eq. (1).

described in Sections 5.2 and 5.3. The significance of the BRDF is that, once obtained for a given surface at a given wavelength and state of polarization, it can be used to compute all other surface optical properties at that wavelength and for that polarization. For example, for a given polarization, the directional spectral absorptance is

$$\alpha_\lambda\left(\lambda, \vartheta_i\right) = 1 - \rho_\lambda\left(\lambda, \vartheta_i\right), \qquad (2a)$$

where

$$\rho_\lambda\left(\lambda, \vartheta_i\right) = \int_0^{2\pi} \int_0^{\pi/2} \rho_\lambda\left(\lambda, \vartheta_i, \vartheta_r, \varphi_r\right) \cos\vartheta_r \sin\vartheta_r \mathrm{d}\vartheta_r \mathrm{d}\varphi_r \qquad (2b)$$

is the directional-hemispherical reflectivity. In Eq. (2b), $\rho_\lambda(\lambda, \vartheta_i, \vartheta_r, \varphi_r)$ is the BRDF, BRDF$(\lambda, \vartheta_i, \vartheta_v, \varphi_v)$, where (ϑ_v, φ_v) is the viewing direction.

The absence of the incident azimuth angle φ_i in the argument lists in Eqs. (2) reflects the fact that gold-black, like many surfaces of usual engineering interest, is isotropic. Because our apparatus only measures the variation of BRDF with reflected zenith angle ϑ_r for a given value of ϑ_i, our results should properly be referred to as in-plane BRDF measurements.

B. Apparatus for Measuring in-Plane BRDF

The automated bench-level gonioreflectometer used to measure the in-plane BRDF of our gold-black samples, shown schematically in Fig. 5, is described in more detail elsewhere [31–33]. Briefly, two precision rotation stages are assembled coaxially and are controlled by high-precision stepper motors commanded by LabView software. The first rotational stage motor rotates the sample holder, while the second stage motor rotates the arm carrying a photodetector. Stationary laser sources illuminate the sample through an optical train. Rotating the sample varies the angle of incidence of the laser beam. Once the sample is illuminated by the laser source, the first stage is commanded via LabView to rotate the sample to a specified incidence angle. Then the second stage is commanded to rotate the photodetector to a set of specified discrete viewing angles in the plane of incidence. The photodetector then orbits the sample in the plane of incidence and senses the reflected intensity in that plane. LabView simultaneously logs the angular position of both the sample and the detector and the output of the photodetector. Additional details are available in the cited references.

The intensity and polarization of the incident laser beam are controlled by a half-wave plate and a polarizing beam splitter.
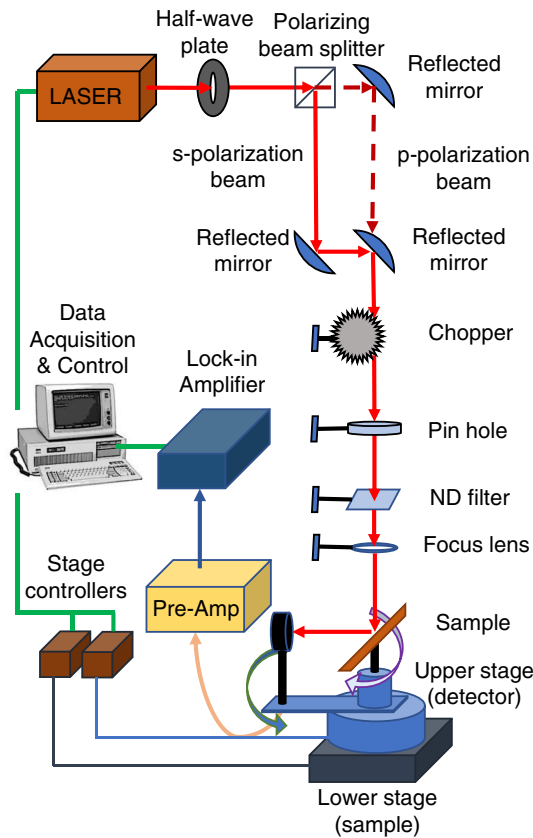
Fig. 5. Schematic diagram of the automated gonioreflectometer used to measure the BRDF of our gold-black samples [31–33].

A 200-µm slit is mounted as a field stop on the entrance aperture of the photodetector. The area of the slit and the length of the arm carrying the detector determine the solid angle of the reflected beam for the measurements. A rotating disc optical chopper is synced with a lock-in amplifier to modulate the intensity of the beam and to diminish the effects of ambient light fluctuations. The chopping frequency is sufficiently high to compensate for drift in the signal-conditioning electronics. Additional auxiliary components such as iris diaphragms, beam-steering mirrors, neutral-density filters, and a periscope are used to guide a collimated and linearly polarized circular laser beam to the sample.

C. Procedure for Measuring in-Plane BRDF

The BRDF of our gold-black samples was measured in the visible (532 nm) and near infrared (800 nm). A power-stabilized 532-nm (green) diode laser was the visible light source, and a tunable Ti-sapphire laser with a wavelength range of 750 to 850 nm was the source of near-infrared light. After securing the gold-black sample in place, it was illuminated with the laser, and proper alignment was achieved. Extreme caution was maintained while handling the gold-black sample due to its fragile nature. The power of the beam was controlled by a half-wave plate and a neutral-density filter, and it was maintained at a level sufficiently low to avoid damaging the sample. This range was established experimentally by exposing a sample to the laser

beam for several hours followed by inspection with a visible-light microscopic. The beam power was measured by a power meter after installation of each component of the optical train to verify that it remained constant during buildup and alignment. As a calibration, the beam was allowed to directly illuminate the photodetector to verify that it produced the same reading as the power meter. The polarization state of the laser was controlled by appropriate orientation of the polarizing beam splitter cube for each wavelength range.

Although the incident zenith angle can be varied from 0 to 110 deg, in the current study measurements were obtained every 10 degrees from 10 to 50 deg. Once the sample has been positioned and illuminated at its center, the first stage is commanded via LabView to rotate the sample to a specified incident zenith angle. The second stage is then commanded to orbit the sample in order to detect the reflected beam over a specified range of viewing zenith angles in the plane of incidence. At each combination of incident zenith angle and viewing zenith angle, LabView logs the sample and the detector positions and the power incident to the photodetector. The beam reflected from the sample is expected to be more powerful at viewing zenith angles near the specular peaks. Therefore, data are first collected to locate the specular peak, and then for viewing zenith angles within a limited range surrounding the specular peak. As explained in Section 5, specular peaks are observed only when coating samples are optically thin for a given wavelength, polarization state, or incident zenith angle.

The design of the reflectometer is such that the BRDF is related to the measurements according to [30]

$$\mathrm{BRDF} = \frac{P_d / P_s}{\Omega \cos\theta}, \tag{3}$$

where P_d is the power of the reflected beam detected by the photodetector, P_s is the power incident to the sample, and Ω is the solid angle established by the area of the slit mounted on the entrance aperture of the photodetector and the sample-detector distance. The same procedure was followed in order to obtain the BRDF measurement of both the coated and uncoated gold-plated substrate.

6. BIDIRECTIONAL REFLECTANCE

Figure 6 shows the instrument noise-equivalent BRDF corresponding to the case of zero laser power (i.e., when the laser is turned off). This measurement was repeated before and after each data-collection run to assure system stability. The result shown in Fig. 6 is typical. Starting with a 0-deg value of $0.01 \, \mathrm{sr}^{-1}$, the noise-equivalent BRDF is seen to vary with viewing zenith angle at a rate of $0.0002 \, \mathrm{sr}^{-1}\mathrm{deg}^{-1}$, with roughly an order-of-magnitude scatter about the local mean. This imposes a lower limit of about $0.05 \, \mathrm{sr}^{-1}$ on the relevance of BRDF measurements obtained using this apparatus in the 0-to-50-deg viewing zenith angle range.

Figure 7 shows the in-plane BRDF of the uncoated pure gold substrate layer in the visible (532 nm, p and s polarization) and near-IR (800 nm, p and s polarization) at incident zenith angles of 10, 20, 30, 40, and 50 deg. The substrate BRDF results are similar in that they all exhibit a narrow specular peak that
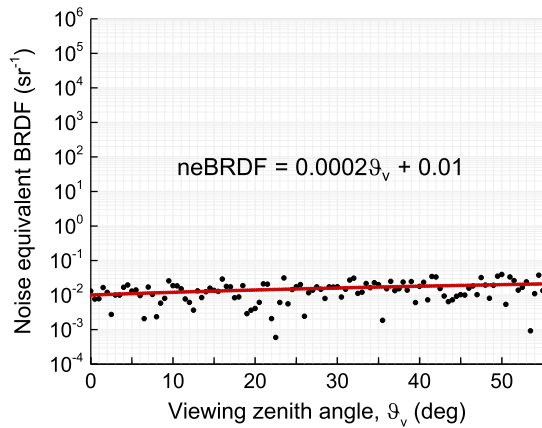
Fig. 6. Noise-equivalent BRDF measurement typical of those obtained before and after each data run, i.e., for each combination of gold-black sample thickness, wavelength, and polarization state.

abruptly broadens into a glossy skirt about 4 orders of magnitude below the peak and 2 orders of magnitude above a diffuse floor. The peak values of BRDF for the gold-mirror substrate are observed to increase slightly with incident zenith angle for both wavelengths. The BRDF of pure gold in the visible is lower than in the near-IR.

Figure 8 summarizes the measured BRDF for the 4-μm-thick layer of gold-black deposited on a gold substrate in the visible and near-IR for both *p* and *s* polarization at incident zenith angles of 10, 20, 30, 40, and 50 deg. The sharp peaks at viewing angles corresponding to the five incident zenith angles represent power that has passed through the gold-black layer, been reflected by the gold substrate, and then passed through the gold-black layer a second time. Because the gold-black layer is relatively thin, the shapes of the peaks in Fig. 8, including the glossy skirts, correspond to attenuated versions of the peaks in Fig. 7 for the uncoated substrate. The peak values themselves exceed by about 4 orders of magnitude the highest BRDF values in their corresponding glossy skirts. This suggests that, compared to absorption, scattering of power out of the beam as it traverses the gold-black layer twice contributes little to beam attenuation. We conclude that the difference in corresponding peak values in Figs. 7 and 8 is due mostly to absorption in the gold-black layer.

Figure 9 summarizes the measured BRDF for the 8-μm-thick layer of gold-black deposited on a pure gold substrate in the visible and near-IR for both *p* and *s* polarization at incident zenith angles of 10, 20, 30, 40, and 50 deg. The specular peaks that dominate the BRDF in Fig. 8 are conspicuously absent in Figs. 9(a)–9(c), i.e., absorption in the thicker layer is nearly complete in this range of incident zenith angles. The very narrow BRDF peak at 50 deg for *p* polarization [Fig. 9(c)] is unexpected and is likely a measurement artefact. Because the spot size on the sample increases with increasing incident angle, illumination might have spilled over onto a flaw in the gold-black layer during the measurement at 50 deg.
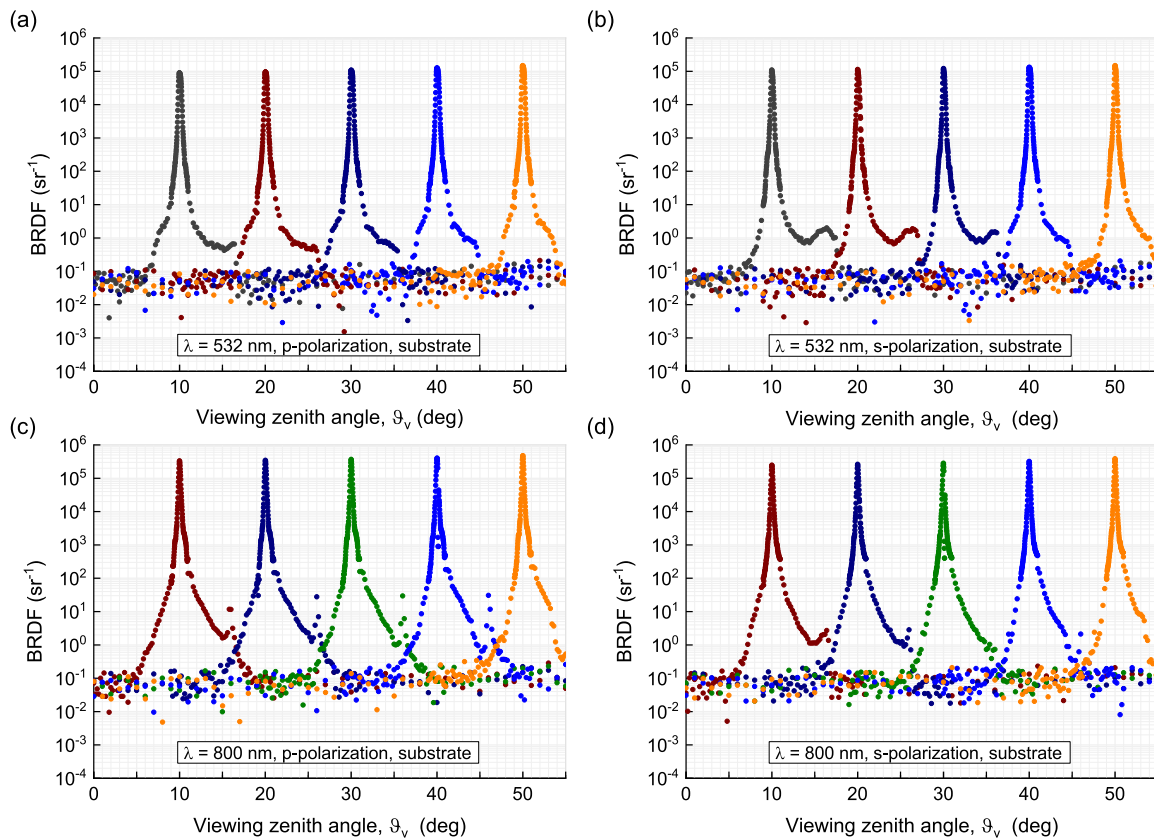

Fig. 7. BRDF of the uncoated pure gold substrate layer in the visible at $\lambda = 532$ nm for (a) *p* polarization and (b) *s* polarization at incident zenith angles of 10, 20, 30, 40, and 50 deg. BRDF of the uncoated pure gold substrate layer in the near-IR at $\lambda = 800$ nm for (c) *p* polarization and (d) *s* polarization at incident zenith angles of 10, 20, 30, 40, and 50 deg.
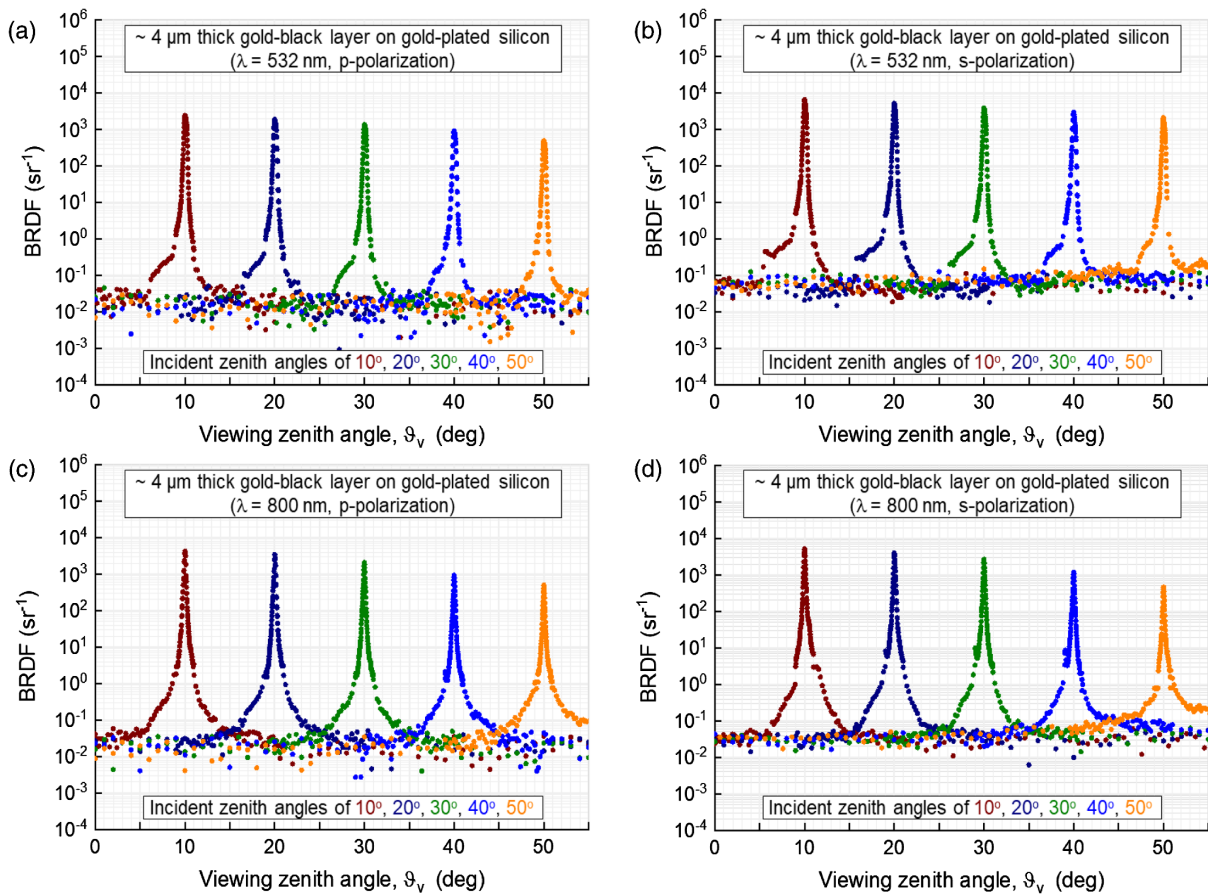
Fig. 8. Measured BRDF corresponding to an approximately 4-μm-thick gold black layer deposited on a pure gold substrate in the visible at $\lambda = 532$ nm for (a) p polarization and (b) s polarization at incident zenith angles of 10, 20, 30, 40, and 50 deg. Measured BRDF corresponding to an approximately 4-μm-thick gold black layer deposited on a pure gold substrate in the near-IR at $\lambda = 800$ nm for (c) p polarization and (d) s polarization at incident zenith angles of 10, 20, 30, 40, and 50 deg.

The hint of a peak corresponding to an incident zenith angle of 10 deg in Fig. 9(a) occurs because the total beam path length through the layer, $L = 2t/\cos(\vartheta_i)$, is shortest at this zenith angle. The effect of increasing beam path length with incident zenith angle also accounts for the slight but discernible decrease in the diffuse component of BRDF with increasing incident zenith angle. Figure 9(a) reveals that absorption is so complete that the measured BRDF essentially lies at the noise floor. Comparison of Figs. 9(a) and 9(b) reveals that gold-black absorbs p-polarized visible light more efficiently than s-polarized visible light by nearly an order of magnitude.

The absence of specular peaks in Fig. 9(b) and their presence in Fig. 9(d) may be explained by the fact that the reflectivity of the pure gold substrate is greater in the near-IR than in the visible, as is evident in Fig. 7. Comparison of Figs. 9(c) and 9(d) makes it clear that, in the near-IR, gold-black is a more efficient absorber of p-polarized light than s-polarized light as predicted by the dipole antenna theory developed in Ref. [9]. In the cited reference, gold-black is modeled as a collection of gold nanowires that behave as dipole antennas; on average, the density of the vertical nanowires is shown to exceed that of the horizontal nanowires in the cited reference.

7. DIRECTIONAL ABSORPTANCE

The ratio of the peak value of BRDF for a gold-black layer laid down on a gold substrate to the corresponding peak value of BRDF for the uncoated gold substrate, $\mathrm{BRDF}_{gb+s}/\mathrm{BRDF}_s$, is indicative of the transmittance of the gold-black layer. This is especially true when the specular peaks exceed the glossy and diffuse components from which they rise by several orders of magnitude, as is the case in Fig. 8 and to a lesser extent in Fig. 9(d). For a single passage of light through the coating,

$$\alpha + \sigma_b + \sigma_f + \tau = 1, \tag{4}$$

where the absorptance α is the fraction of incident power absorbed within the gold-black, σ_b is the fraction of incident power that is backscattered, σ_f is the fraction of incident power that is forward scattered, and τ is the fraction of the incident power that is neither absorbed nor scattered, i.e., that is transmitted. A more traditional version of Eq. (4), written from the perspective of the upper surface of the coating, would identify σ_b as the fraction ρ of the incident power reflected from the surface and would combine σ_f and τ into a single transmittance term. The fact that the peaks in Figs. 8 and 9(d) rise several orders of magnitude above the glossy and diffuse scattered components justifies suppressing σ_b and
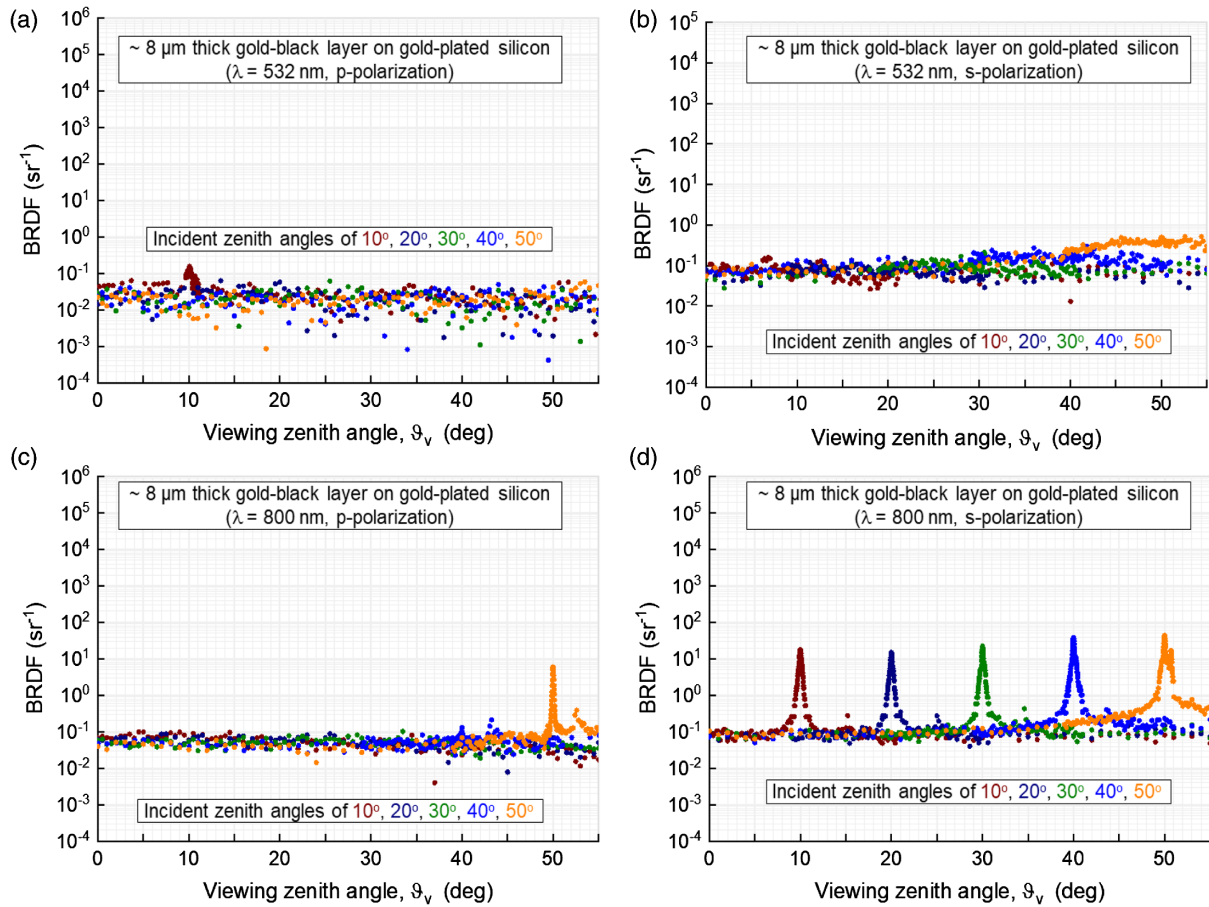
Fig. 9. Measured BRDF corresponding to an approximately 8-μm-thick gold black layer deposited on a pure gold substrate in the visible at $\lambda = 532$ nm for (a) *p* polarization and (b) *s* polarization at incident zenith angles of 10, 20, 30, 40, and 50 deg. Measured BRDF corresponding to an approximately 8-μm-thick gold black layer deposited on a pure gold substrate in the near-IR at $\lambda = 800$ nm for (c) *p* polarization and (d) *s* polarization at incident zenith angles of 10, 20, 30, 40, and 50 deg.

σ_f in Eq. (4), so that at the specular peaks we have, to a good approximation,

$$\tau \cong 1 - \alpha. \tag{5}$$

Neglecting scattered radiation, the peak value of BRDF corresponding to a gold-black-coated gold mirror is proportional to $(I_i \tau \rho_s) \tau$, where I_i is the incident radiance and ρ_s is the reflectivity of the gold substrate. The factor τ appears twice in this expression because the incident radiation traverses the gold-black layer two times. The peak value of BRDF corresponding to the uncoated substrate is proportional to $I_i \rho_s$. The ratio $\mathrm{BRDF}_{gb+s} / \mathrm{BRDF}_s$ is then τ^2 which, from Eq. (5), is well approximated as $(1 - \alpha)^2$. Therefore, to an acceptable approximation, the absorptance of a gold-black layer of a given thickness for a given wavelength, polarization state, and incident zenith angle is

$$\alpha \cong 1 - \sqrt{\mathrm{BRDF}_{gb+s} / \mathrm{BRDF}_s}. \tag{6}$$

For a given incident zenith angle ϑ_i, the path length traversed by the beam through the gold-black layer is

$$L = 2t / \cos(\vartheta_i), \tag{7}$$

where t is the layer thickness.

Figure 10 shows the variation of absorptance as computed using Eq. (6), with path length as computed using Eq. (7), based on BRDF measurements for the 4-μm-thick gold-black sample given in Fig. 8 ($L < 13$ μm) and for the 8-μm-thick gold-black sample given in Fig. 9(d) ($L > 16$ μm). Note that the minimum value on the vertical axis is 0.75. The open symbols represent *p*-polarization results, and the closed symbols represent *s*-polarization results. It is clear that gold-black absorbs *p*-polarized light more efficiently than *s*-polarized light, a result predicted by the theory of Ref. [9].

Figure 10 indicates that this form of gold-black is a more efficient absorber in the near-IR than in the visible. The theory of Ref. [9] is reticent on gold-black absorptance in the visible; however, it does predict that the single-filament spectral absorptance of gold-black decreases with the value of the nondimensional parameter

$$M = \frac{\sigma_1}{\varepsilon_1} \frac{\Delta x n_1}{c_0}, \tag{8}$$

where σ_1 is the real part of the complex electrical conductivity of gold, ε_1 is the real part of its dielectric function, Δx is the calculation mesh size in a finite-difference time-dependent (FDTD)
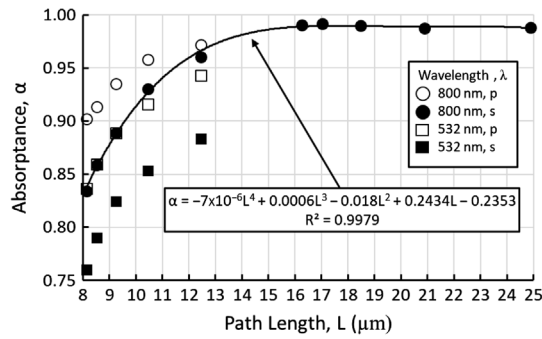
Fig. 10. Variation of absorptance at 532 and 800 nm as computed using Eq. (6), with path length, as computed using Eq. (7), based on the BRDF measurements given in Figs. 8 and 9(d).

Fig. 11. Variation of single-strand absorptance with the M parameter as predicted by the near-IR theory of Ref. [9] (open symbols) and as extended to the visible (closed symbol).

lossy dipole antenna model, n_1 is the real part of its complex refractive index, and c_0 is the speed of light in a vacuum. The mesh size Δx is proportional to the overall filament length and so is a characteristic length of the model. In the cited theory, the values of σ_1, ε_1, and n_1 are computed using Drude–Sommerfeld free-electron theory, which is shown to be in good agreement with experimental values for wavelengths longer than those corresponding to the plasma frequency of pure gold. However, below the plasma frequency the values of σ_1 and n_1 deviate sharply from Drude–Sommerfeld theory as shown in Fig. 5 of Ref. [9]. The wavelength corresponding to the plasma frequency of pure gold lies between the two wavelengths investigated here. Therefore, in its original form the theory presented in Ref. [9] cannot be used to predict the absorptivity of gold-black at 532 nm.

The dipole antenna theory of Ref. [9] has been used to compute the absorptance α_1 of a single gold nanostrand of length $L = 800$ nm at wavelengths of 800, 1400, and 2800 nm. The results are plotted in Fig. 11 against the M parameter computed using the Drude–Sommerfeld values of the optical and electrical properties (open symbols). The M parameter has also been evaluated at 532 nm using the experimental values for the optical and electrical properties given by Olmon *et al.* [34]. A power-law fit to the open symbols has been extrapolated to the value of the M parameter corresponding to 532 nm. If, as suggested by the authors of Ref. [9], the cited theory can reliably be extended to shorter wavelengths using experimental values of the optical and electrical properties, then the theory predicts that the absorptivity in the visible should be less than that in the near-IR.

The specular peaks in Fig. 9(d) for the 8-μm-thick sample allow calculation of gold-black absorptance over an extended path length range. The line in Fig. 10 passing through the solid circular symbols corresponding to s-polarized light at 800 nm is a fourth-order polynomial. From this curve we may conclude that a gold-black layer about 15 μm thick is for all practical purposes "infinitely thick" with an absorptance of about 0.99 for s-polarized radiation at 800 nm. The trend for the p-polarization results at this wavelength (open circular symbols) suggests a convergence to the same asymptotic value. That is, even though gold-black is a more efficient absorber of p-polarized radiation than s-polarized radiation, this difference diminishes as the asymptotic layer thickness is approached.
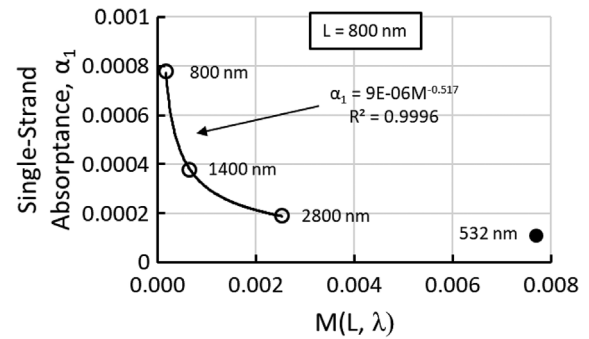
8. CONCLUSIONS AND RECOMMENDATIONS

New in-plane BRDF measurements for two thicknesses (∼4 μm and ∼8 μm) of gold-black deposited on a gold substrate are presented for p- and s-polarized light in the visible (532 nm) and near-infrared (800 nm). The equipment and procedure used to create the gold-black samples and to obtain the in-plane BRDF measurements are described. The BRDF measurements are interpreted in terms of absorptance. Absorptance results for p and s polarization in the near-IR are found to be in good agreement with those anticipated by our earlier theory [9]. Specifically, measurements verify that gold-black absorbs p-polarized light more efficiently than s-polarized light in the wavelength interval spanning the visible and near-IR. Evidence is presented that the cited theory can be extended into the visible if measured values of the optical and electrical constants are used in place of those obtained using Drude–Sommerfeld theory. Results suggest that gold-black coatings on thermal radiation detectors intended for use in the visible and near-IR should be applied to a thickness of at least 15 μm.

Disclosures. The authors declare no conflict of interest.

Data Availability. Data underlying the results presented in this paper are not publicly available at this time but may be obtained from the corresponding author upon reasonable request.

REFERENCES

1. A. J. Illingworth, H. W. Barker, A. Beljaars, M. Ceccaldi, H. Chepfer, N. Clerbaux, J. Cole, J. Delanoe, C. Domenech, D. P. Donovan, S. Fukuda, M. Hirakata, R. J. Hogan, A. Huenerbein, P. Kollias, T. Kubota, T. Nakajima, T. Y. Nakajima, T. Nishizawa, Y. Ohno, H. Okamoto, R. Oki, K. Sato, M. Satoh, M. W. Shephard, A. Velazquez-Blazquez, U. Wandinger, T. Wehr, and G.-J. van Zadelhoff, "The EarthCARE satellite: the next step forward in global measurements of clouds, aerosols, precipitation, and radiation," Bull. Am. Meteorol. Soc. **96**(8), 1311–1332 (2015).
2. B. A. Wielicki, B. R. Barkstrom, E. F. Harrison, R. B. Lee, III, G. L. Smith, and J. E. Cooper, "Clouds and the Earth's radiant energy system (CERES): an Earth observing system experiment," Bull. Am. Meteorol. Soc. **77**(8), 853–868 (1996).

3. E. Georgieva, K. Priestley, B. Dunn, R. Cageao, A. Barki, J. Osmundsen, C. Turczynski, and N. Abedin, "Radiation budget instrument (RBI) for JPSS-2," in *24th Conference on Characterization and Radiometric Calibration for Remote Sensing (CALCON)* (Space Dynamics Laboratory/Utah State University, 2015).

4. G. Taylor, and NASA Earth Science Technology Office, "Small sensor could provide big insights into Earth's radiation budget," 2021, https://esto.nasa.gov/demeter/.

5. A. Pfund, "Bismuth black and its applications," Rev. Sci. Instrum. **1**, 397–399 (1930).

6. A. Pfund, "The optical properties of metallic and crystalline powders," J. Opt. Soc. Am. A **23**, 375–378 (1933).

7. Y. Hao, S. H. Yang, Z. Li, X. Wang, J. Y. Zhang, Y. Q. Liao, and D. F. Li, "Ultrabroadband metal-black absorbers and the performance simulations based on a three-dimensional cluster-structure model," Opt. Express **29**, 8510–8522 (2021).

8. R. E. Peale, "Long-wave and mid-wave infrared micro-bolometers with gold black or wavelength-selective absorbers," Proc. SPIE **10656**, 10656B (2018).

9. N. B. Munir, J. R. Mahan, and K. J. Priestley, "First-principle model for the directional spectral absorptivity of gold-black in the near infrared," J. Opt. Soc. Am. A **36**, 1675–1689 (2019).

10. L. Harris, R. T. McGinnies, and B. M. Siegel, "The preparation and optical properties of gold blacks," J. Opt. Soc. Am. **38**, 582–589 (1948).

11. L. Harris, D. Jeffries, and B. M. Siegel, "An electron microscope study of gold smoke deposits," J. Appl. Phys. **19**, 791–794 (1948).

12. L. Harris and J. K. Beasley, "An electron microscope study of gold smoke deposits," J. Opt. Soc. Am. **42**, 134–140 (1952).

13. L. Harris and A. L. Loeb, "Conductance and relaxation time of electrons in gold blacks from transmission and reflection measurements in the far infrared," J. Opt. Soc. Am. **43**, 1114–1118 (1953).

14. L. Harris and K. F. Cuff, "Reflectance of goldblack deposits, and some other materials of low reflectance from 254 mμ to 1100 mμ. The scattering-unit-size in goldblack deposits," J. Opt. Soc. Am. **46**, 160–163 (1956).

15. G. Zaeschmar and A. Nedoluha, "Theory of the optical properties of gold blacks," J. Opt. Soc. Am. **62**, 348–352 (1972).

16. P. O'Neill, C. Doland, and A. Ignatiev, "Structural composition and optical properties of solar blacks: gold black," Appl. Opt. **16**, 2822–2826 (1977).

17. P. O'Neill, A. Ignatiev, and C. Doland, "The dependence of optical properties on the structural composition of solar absorbers: gold black," Sol. Energy **21**, 465–468 (1978).

18. W. Lang, K. Kühl, and H. Sandmaier, "Absorbing layers for thermal infrared detectors," Sens. Actuators A **34**, 243–248 (1992).

19. W. Becker, R. Fettig, A. Gaymann, and W. Ruppel, "Black gold deposits as absorbers for far infrared radiation," Phys. Status Solidi B **194**, 241–255 (1996).

20. W. Becker, R. Fettig, and W. Ruppel, "Black gold deposits as absorbers for far infrared radiation," Infrared Phys. Technol. **40**, 431–445 (1999).

21. J. Lehman, E. Theocharous, G. Eppeldauer, and C. Pannell, "Gold-black coating for freestanding pyroelectric detectors," Meas. Sci. Technol. **14**, 916 (2003).

22. N. Nelms and J. Dowson, "Goldblack coating for thermal infrared detectors," Sens. Actuators A **120**, 403–407 (2005).

23. S. Ilias, P. Topart, C. Larouche, P. Beaupré, D. Gay, C. Proulx, T. Pope, and C. Alain, "Deposition and characterization of gold black coatings for thermal infrared detectors," Proc. SPIE **7750**, 77501J (2010).

24. B. Wang, J. Lai, S. Chen, E. Zhao, H. Hu, and Q. Lu, "Vanadium oxide microbolometer with gold black absorbing layer," Opt. Eng. **51**, 074003 (2012).

25. D.-P. Qian, C.-G. Wu, Y. Shuai, W.-B. Luo, Q.-X. Peng, X.-Y. Chen, and W.-L. Zhang, "Hardening and optimizing of the black gold thin film as the absorption layer for infrared detector," Opt. Photon. J. **3**, 281–283 (2013).

26. D. Panjwani, M. Yesiltas, S. Singh, E. Del Barco, R. Peale, C. Hirschmugl, and J. Sedlemair, "Stencil lithography of gold-black IR absorption coatings," Infrared Phys. Technol. **66**, 1–5 (2014).

27. D. Panjwani, "Characterization of gold black and its application in uncooled infrared detectors," Ph.D. dissertation (University of Central Florida, 2015).

28. E. M. Smith, D. Panjwani, J. Ginn, A. P. Warren, C. Long, P. Figuieredo, C. Smith, J. Nath, J. Perlstein, and N. Walter, "Dual band sensitivity enhancements of a VOx microbolometer array using a patterned gold black absorber," Appl. Opt. **55**, 2071–2078 (2016).

29. C. Ng, L. W. Yap, A. Roberts, W. Cheng, and D. E. Gómez, "Black gold: broadband, high absorption of visible light for photochemical systems," Adv. Funct. Mater. **27**, 1604080 (2017).

30. J. R. Mahan, *The Monte Carlo Ray-Trace Method in Radiation Heat Transfer and Applied Optics* (Wiley, 2019).

31. L. C. Doan, J. R. Mahan, K. J. Priestley, and N. Q. Vinh, "Measuring bidirectional reflectance distribution of low reflectivity surfaces in the near infrared," Proc. SPIE **11103**, 111030I (2019).

32. D. Shirsekar, Y. Wang, J. R. Mahan, K. J. Priestley, and V. Q. Nguyen, "Bidirectional reflectance measurement of black absorber layers for use in optical instrument design," Proc. SPIE **10743**, 1074303 (2018).

33. D. Shirsekar, N. Vinh, J. R. Mahan, and K. J. Priestley, "Design and demonstration of an automated bidirectional reflectometer for low-reflectivity optical coatings," in *ASTFE Digital Library* (Begel House Inc., 2019), pp. 941–947

34. R. L. Olmon, B. Slovick, T. W. Johnson, D. Shelton, S.-H. Oh, G. D. Boreman, and M. B. Raschke, "Optical dielectric function of gold," Phys. Rev. B **86**, 235147 (2012).